STRUCTURAL BIOLOGY

Cryo-EM structures of the human surfactant lipid transporter ABCA3

Tian Xie†, Zike Zhang†, Jian Yue†, Qi Fang, Xin Gong*

The adenosine 5′-triphosphate (ATP)–binding cassette (ABC) transporter ABCA3 plays a critical role in pulmonary surfactant biogenesis. Mutations in human ABCA3 have been recognized as the most frequent causes of inherited surfactant dysfunction disorders. Despite two decades of research, in vitro biochemical and structural studies of ABCA3 are still lacking. Here, we report the cryo-EM structures of human ABCA3 in two distinct conformations, both at resolution of 3.3 Å. In the absence of ATP, ABCA3 adopts a "lateral-opening" conformation with the lateral surfaces of transmembrane domains (TMDs) exposed to the membrane and features two positively charged cavities within the TMDs as potential substrate binding sites. ATP binding induces pronounced conformational changes, resulting in the collapse of the potential substrate binding cavities. Our results help to rationalize the disease-causing mutations in human ABCA3 and suggest a conserved "lateral access and extrusion" mechanism for both lipid export and import mediated by ABCA transporters.

INTRODUCTION

Pulmonary surfactant, a mixture of approximately 90% lipids and 10% proteins, is secreted by the alveolar type II (AT2) epithelial cells and dedicated to maintain the normal breathing by reducing alveolar surface tension (*1*–*3*). Before secretion, the pulmonary surfactant is stored in AT2 cell–specific, multilamellated lysosome-derived organelles named lamellar bodies (LBs) (*4*, *5*). ABCA3 is localized in the limiting membrane of LBs and participates in surfactant biogenesis by transporting surfactant lipids, such as phosphatidylcholine (PC), phosphatidylglycerol (PG), and cholesterol, into LBs (Fig. 1A) (*6*–*14*). Mutations in ABCA3 gene may cause surfactant deficiency, which leads to various lung disorders, such as fatal neonatal surfactant deficiency, chronic interstitial lung disease, and diffuse parenchymal lung disease (*15*–*17*). To date, no specific therapies exist for the hereditary disorders caused by ABCA3 mutations. Three-dimensional (3D) structural information of ABCA3 would help to rationalize the disease-causing mutations with the final aim of developing therapies for patients.

Human ABCA3, consisting of 1704–amino acid residues, can be divided into two homologous halves, each half harboring one transmembrane domain (TMD1/TMD2), one exocytosolic domain (ECD1/ECD2), one nucleotide-binding domain (NBD1/NBD2), and one regulatory domain (RD1/RD2) (Fig. 1B) (*18*, *19*). ABCA3 belongs to the ABCA transporter subfamily, which consists of 12 structurally related transporters in humans (*20*–*23*), and was classified as type V adenosine 5′-triphosphate (ATP)–binding cassette (ABC) transporters based on their structure and transmembrane (TM) fold (*24*–*26*). The ECDs and RDs are unique for the ABCA subfamily, not presented in any other ABC transporters (*19*). ECD1 and ECD2 are most variable among the ABCA transporters, accounting for the diversity and different lengths of human ABCA transporters (ranging from 1543 to 5058 amino acids) (*19*, *20*). The ECDs of ABCA3 are far shorter than those of structurally characterized ABCA1, ABCA4, and ABCA7 (fig. S1) (*27*–*31*). The ECD1 of ABCA3 undergoes a unique proteolytic processing near Lys^{174} (Fig. 1B), generating a protein band shortened by ~20 to 40 kDa (*32*, *33*). However, the purpose of this processing remains to be elucidated.

Like most eukaryotic ABC transporters, all the ABCA transporters except ABCA4 are thought to function as "exporters" that translocate the substrates from the cytosolic leaflet to the exocytosolic (extracellular or luminal) leaflet of membranes (*8*, *34*). ABCA4, the only "importer" among the ABCA subfamily transporters, translocates substrates in an opposite direction (*34*, *35*). Recently, cryo–electron microscopy (cryo-EM) structures of the lipid importer ABCA4 in both "lateral-opening" conformation (apo- or substrate-bound states) and "closed" conformation (ATP-bound state) were reported (*28*–*30*), suggesting a "lateral access and extrusion" mechanism for substrate import (*30*). Nevertheless, the structures of lipid exporter ABCA1 and ABCA7 were only resolved in the lateral-opening conformation (*27*, *31*). Structures of ABCA transporters, especially exporters, in different conformations during a transport cycle are essential to understand the lipid transport mechanism.

Despite the critical roles of ABCA3 in physiology and pathophysiology, in vitro biochemical and structural characterizations of ABCA3 are still lacking. In the present study, we purified and biochemically characterized human ABCA3 proteins in different processed states and solved the cryo-EM structures of ABCA3 in two distinct conformations. The structures reveal two positively charged cavities within the TMDs as the potential substrate binding sites and delineate the ATP-dependent conformational changes to export the lipid substrates across the membrane, suggesting a conserved lipid transport mechanism for both lipid export and import mediated by ABCA transporters.

RESULTS

Biochemical characterization of human ABCA3

The details of recombinant expression and purification of the full-length (FL) human ABCA3 in human embryonic kidney (HEK) 293F cells can be found in Materials and Methods. The ABCA3 protein was extracted from the membrane using a mixture of lauryl maltose neopentyl glycol (LMNG) and cholesteryl hemisuccinate (CHS), which were exchanged to glyco-diosgenin (GDN) detergent

Department of Biology, School of Life Sciences, Southern University of Science and Technology, Shenzhen 518055, Guangdong, China.
*Corresponding author. Email: gongx@sustech.edu.cn
†These authors contributed equally to this work.

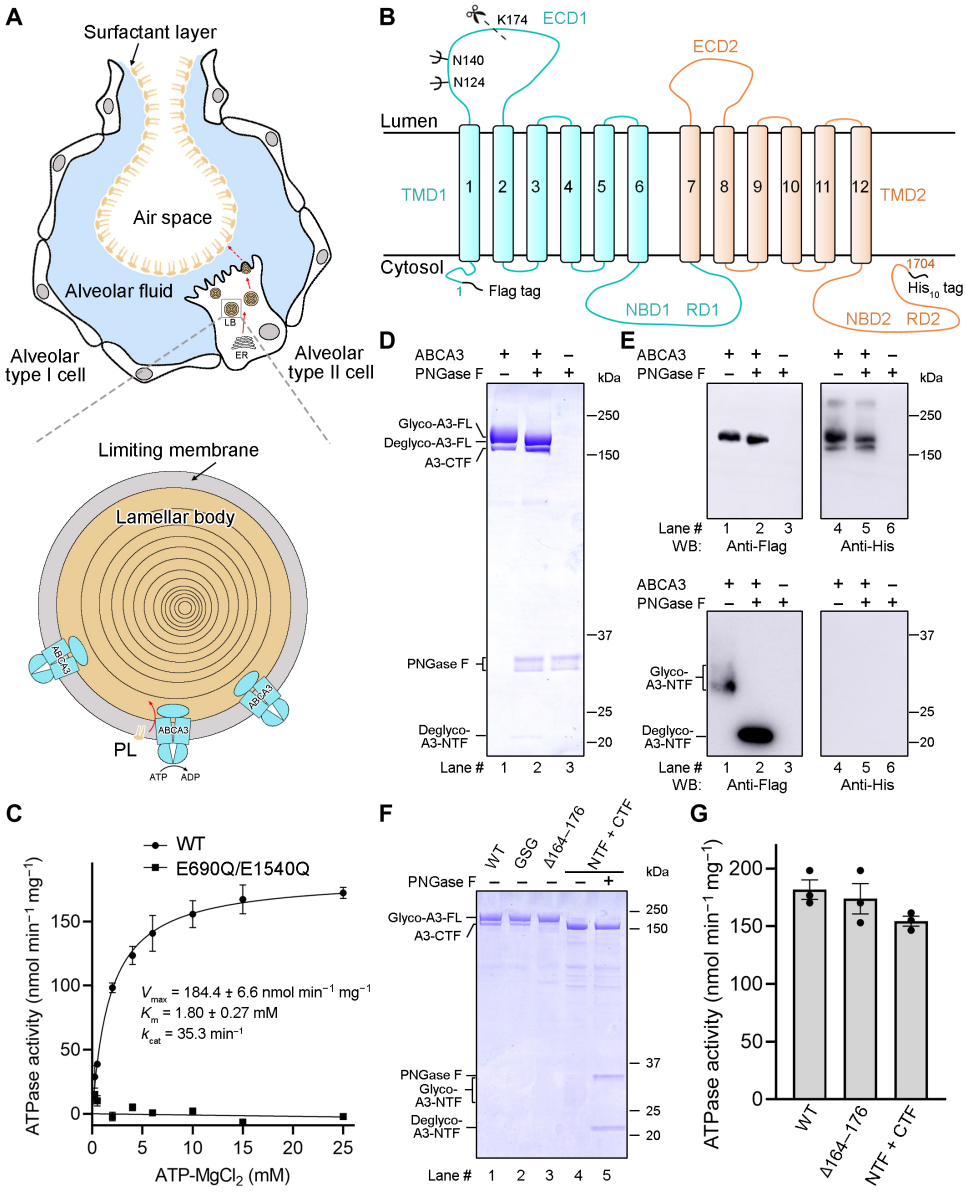

Fig. 1. Biochemical characterization of human ABCA3. (**A**) A schematic diagram of the pulmonary alveolus and LB. The alveolar surface mainly consists of AT1 and AT2 cells. The AT2 cells are involved in the production, storage, secretion, and recycling of pulmonary surfactant. The surfactant components are synthesized in the endoplasmic reticulum (ER) and trafficked mainly to the LBs. The intracellular lipid transporter ABCA3, located in the limiting membrane of LBs, functions to translocate surfactant lipids, such as phospholipids (PLs), from the cytosolic leaflet into the LB lumen upon ATP hydrolysis. ADP, adenosine 5′-diphosphate. (**B**) Topological diagram of human ABCA3. Human ABCA3 was fused with an N-terminal Flag tag and a C-terminal His_{10} tag. The N-linked glycosylation sites at residues Asn^{124} and Asn^{140} and the cleavage site around Lys^{174} are presented. TMD, transmembrane domain; ECD, exocytosolic domain; NBD, nucleotide-binding domain; RD, regulatory domain. (**C**) Specific adenosine triphosphatase (ATPase) activity versus ATP concentration measured using wild-type (WT) ABCA3 protein or the catalytic mutant (E690Q/E1540Q). (**D** and **E**) Glycosylation and proteolytic cleavage of ABCA3. The recombinantly expressed and purified ABCA3 was partially cleaved into an N-terminal fragment (NTF) and a C-terminal fragment (CTF). Both the full-length (FL) ABCA3 protein and the NTF were deglycosylated by PNGase F, indicating that the glycosylation sites of ABCA3 are in the NTF. The purified protein was visualized by Coomassie blue–stained SDS–polyacrylamide gel electrophoresis (PAGE) (D) and Western blot (WB) (E). (**F**) Characterization of the proteolytic cleavage sites of ABCA3. GSG represents the L173G/K174S/E175G variant. The coexpressed NTF (1 to 174 amino acids) and CTF (175 to 1704 amino acids) form a stable complex. The NTF was glycosylated and could be deglycosylated by peptide *N*-glycosidase F (PNGase F). (**G**) Functional characterization of the ABCA3 cleavage site variants. The ATPase activity of WT ABCA3 and two variants were measured. For all dot plot graphs, each data point is the average of three independent experiments, and error bars represent the SEM.

during purification. The purified proteins appear to be homogeneous in the detergent-solubilized micelles as examined by size exclusion chromatography (SEC) (fig. S2A). The adenosine triphosphatase (ATPase) activity of ABCA3 was measured as a function of ATP concentration (Fig. 1C). The wild-type (WT) ABCA3 protein shows a K_m (Michaelis constant) of 1.80 ± 0.27 mM for ATP and a V_{max} (maximum rate of reaction) of 184.4 ± 6.6 nmol min^{-1} mg^{-1} (Fig. 1C). The V_{max} is in general agreement with those for ABCA1 and ABCA4

purified in detergent micelles (~100 to 200 nmol min^{-1} mg^{-1}), whereas the K_m for ATP is much higher than those for ABCA1 and ABCA4 (~0.1 to 0.2 mM) (*27*–*30*), suggesting that ABCA3 has a much lower affinity for ATP than ABCA1 and ABCA4. Mutation of the catalytic glutamates in Walker B motifs of NBD1 and NBD2 with glutamines (E690Q/E1540Q) did not affect the protein behavior in SEC but led to a marked decrease of the ATPase activity (Fig. 1C and fig. S2A).

Consistent with the reported proteolytic processing of ABCA3 (*32*, *33*), the purified ABCA3 displayed two protein bands with apparent molecular weights of ~200 and ~170 kDa on the SDS–polyacrylamide gel electrophoresis (PAGE) gel (Fig. 1D, lane 1). After treatment of the purified proteins by peptide *N*-glycosidase F (PNGase F), the ~200-kDa band shifted to a lower band at ~180 kDa, whereas the ~170-kDa band basically remained unchanged (Fig. 1D, lane 2). A small–molecular weight band at ~21 kDa appeared after the PNGase F treatment (Fig. 1D, lane 2). The Western blot data indicate that the ~200-kDa band corresponds to FL ABCA3, as it contains both the N-terminal Flag tag and C-terminal His tag, the ~170 kDa band corresponds to a cleaved product with only the C-terminal His tag [named C-terminal fragment of ABCA3 (ABCA3-CTF)], and the deglycosylated band at ~21 kDa corresponds to a cleaved product with only the N-terminal Flag tag [named N-terminal fragment of ABCA3 (ABCA3-NTF)] (Fig. 1E). Meanwhile, the glycosylated ABCA3-NTF can be detected near ~30 kDa by the Western blotting (Fig. 1E). These results are consistent with the published proteolytic processing of ABCA3 near Lys^{174} (*32*, *33*) and the experimentally demonstrated N-linked glycosylation at Asn^{124} and Asn^{140} (*36*) (Fig. 1B). Our results suggest that the glycosylated ABCA3 protein can be clipped to produce ~30-kDa ABCA3-NTF and ~170-kDa ABCA3-CTF, which stay together and cofold to form a complete architecture.

To investigate the function of proteolytic processing of ABCA3, we sought to develop a strategy to obtain pure unprocessed and processed ABCA3 preparations. To this end, we generated the following three variants: ABCA3-GSG (mutating the potential cleavage sites near Lys^{174}, L173G/K174S/E175G), ABCA3–Δ164–176 (deleting the whole potential cleavage loop, residues 164 to 176), and ABCA3-NTF + CTF (coexpression of ABCA3-NTF and ABCA3-CTF, residues 1 to 174 and 175 to 1704, respectively). These variants were individually purified to homogeneity and exhibited similar solution behavior as the WT protein (fig. S2B). The ABCA3-L173G/K174S/E175G variant exhibited a similar processing pattern as the WT protein (Fig. 1F, lanes 1 and 2), suggesting the existence of additional cleavage sites beyond the L173/K174/E175. The ABCA3–Δ164–176 variant migrated as a single band similar to the unprocessed FL ABCA3 (Fig. 1F, lane 3), indicating that proteolytic cleavage had been completely abolished. In the purified ABCA3-NTF + CTF variant, a high–molecular weight band corresponding to the ABCA3-CTF was evident at ~170 kDa and a small band corresponding to the ABCA3-NTF can be detected at ~21 kDa upon deglycosylation (Fig. 1F, lanes 4 and 5). Thus, the ABCA3–Δ164–176 and ABCA3-NTF + CTF variants could mimic the pure unprocessed and processed ABCA3, respectively. Nevertheless, the ATPase activities of both variants were comparable to that of the WT protein (Fig. 1G), suggesting that the proteolytic processing of ABCA3 in ECD1 would not allosterically regulate the ATP hydrolysis in NBDs.

Structure of ABCA3 in the nucleotide-free state

The structure of WT ABCA3 was determined by single-particle cryo-EM in the absence of nucleotide to an overall resolution of 3.3 Å (fig. S3). The EM map shows excellent side-chain density and allows model building for most of the protein (fig. S4), except for a few loops (residues 164 to 176, 492 to 515, 858 to 894, 1000 to 1003, 1333 to 1354, and 1699 to 1704). In the final structural model, 1598 residues were built with 1574 side chains assigned, and two sugar moieties were built into the two glycosylation sites (Asn^{124} and Asn^{140}) on ECD1 (table S1). In addition, several strong lipid-like densities that may belong to lipids or detergents were observed between the two TMDs in the cytosolic membrane leaflet (Fig. 2A), which will be discussed in the next section.

The overall structure of ABCA3 exhibits dimensions of approximately 170 Å perpendicular to the membrane and approximately 80 Å parallel to the membrane (Fig. 2A). The two homologous repeats appear to have a twofold pseudosymmetry in the TMD-NBD-RD regions, as they can be superimposed on each other with a root mean square deviation (RMSD) of 2.077 Å over 435 aligned Cα atoms (Fig. 2B). Nevertheless, the two ECDs have broken the pseudosymmetry because they adopt opposite orientations relative to the TMDs (Fig. 2B). The proteolytic cleavage loop (residues 164 to 176) in ECD1 (named C-loop for proteolytic cleavage) was not well resolved in the structure (Fig. 2A), indicating its flexibility, which might facilitate the access of the C-loop by proteases.

The most divergent part among the ABCA3/ABCA4/ABCA1 structures lies in the cofolded ECDs (Fig. 2, C to E). The ECDs of ABCA1 and ABCA4 share a common architecture, which can be allocated into three layers, the "base," the "tunnel," and the "lid" (Fig. 2, D and E) (*27*). By contrast, ABCA3 holds a much smaller ECD, only covering the core region of the base (Fig. 2C). The ECD1 of ABCA3, consisting of 206 amino acids (residues 47 to 252), lacks a ~300–amino acid insertion (ECD1 insertion I) and a ~100–amino acid insertion (ECD1 insertion II), which exist in the ECD1 of ABCA1/ABCA4 (Fig. 2, C to E, and fig. S5A). The ECD2 of ABCA3, consisting of 149 amino acids (residues 946 to 1094), lacks a ~80–amino acid insertion (ECD2 insertion I) and a ~50–amino acid insertion (ECD2 insertion II), which exist in the ECD2 of ABCA1/ABCA4 (Fig. 2, C to E, and fig. S5B). The divergent structures of ABCA-ECD suggest their distinct functional roles among the ABCA subfamily transporters. Several lipid-like densities are evident inside the predominantly hydrophobic tunnel in the resolved ABCA1 and ABCA4 structures (*27*–*30*), suggesting a potential lipid storage or delivery function of the tunnels. Nevertheless, the specific functional role of the ABCA3-ECD, lacking the tunnel and the lid, remains to be determined.

The cytosolic NBDs and RDs are the most conserved elements among ABCA subfamily (*19*). A similar domain-swapped dimer of RDs, with RD1 primarily interacting with NBD2 and RD2 primarily interacting with NBD1, was revealed in the ABCA3 structure as that of ABCA4 (fig. S6, A and B). The structures of NBDs and RDs are largely identical between ABCA3 and ABCA4 with an RMSD of 1.169 Å over 525 aligned Cα atoms (fig. S6C). The NBDs and RDs were assigned as poly-Ala in the ABCA1 structure [Protein Data Bank (PDB) code 5XJY] due to the limited resolution at these regions (fig. S6D). Considering the sequence conservation of the RDs among ABCA subfamily, the RD1 and RD2 initially described in ABCA1 structure were very likely misassigned in a nonswapped configuration in the published structure (fig. S6D) (*27*). The RDs exhibit an ACT-like fold that is typically involved in binding of small regulatory molecules (*28*, *37*). However, whether the ABCA-RDs could bind small molecules and whether this binding would regulate their functions require further investigations.

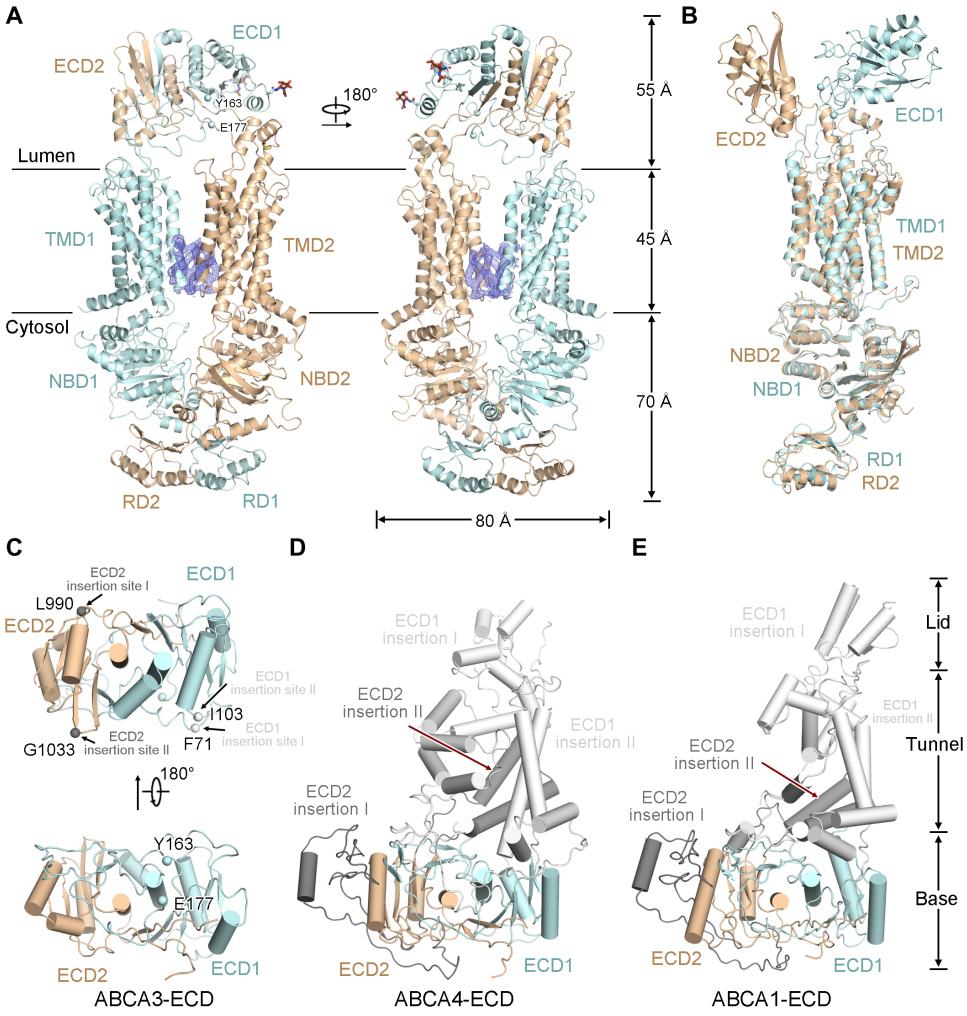

Fig. 2. Overall structure of human ABCA3 in nucleotide-free state. (**A**) Overall structure of ABCA3. The two halves of ABCA3 are colored light cyan and wheat for half 1 (TMD1, ECD1, NBD1, and RD1) and half 2 (TMD2, ECD2, NBD2, and RD2), respectively. The lipid-like density between TMD1 and TMD2 in the cytosolic membrane leaflet are shown as blue mesh, contoured at 3σ. The N-linked glycans are displayed as brown sticks. Residues Tyr^{163} and Glu^{177}, around the boundaries of the cleavage sites, are shown as light cyan spheres. (**B**) Superposition of half 1 (light cyan) and half 2 (wheat) of ABCA3. (**C** to **E**) Close-up views of the ABCA3-ECD (C), ABCA4-ECD (D), and ABCA1-ECD (E). The corresponding regions in the bases of ABCA4-ECD and ABCA1-ECD are in the same coloring scheme as that of ABCA3-ECD. Compared with ABCA3-ECD, both ABCA4-ECD and ABCA1-ECD have four extra insertions (two in ECD1 and the other two in ECD2). The ECD1 insertions I and II in both ABCA4-ECD and ABCA1-ECD are colored light gray. The ECD2 insertions I and II in both ABCA4-ECD and ABCA1-ECD are colored dark gray. The corresponding insertion sites for the extra motifs in ABCA3-ECD1 and ABCA3-ECD2 are shown as light and dark gray spheres, respectively. All structural figures were prepared using PyMol (www.pymol.org/) or UCSF Chimera (*62*).

Two positively charged cavities within the TMDs

The TMDs of ABCA3, each consisting of six TMs, display a typical type V ABC fold without TM segment swapping between the two homologous halves (Fig. 3A) (*27*, *38*, *39*). In the nucleotide-free state, the TMDs of ABCA3 exhibit a similar lateral-opening conformation as the nucleotide-free structures of ABCA1 and ABCA4 (Fig. 3A and fig. S7, A to C) (*27*–*30*). The major differences among the TMDs of ABCA3/ABCA4/ABCA1 lie in the TM8 and the last exocytosolic loop (between TM11 and TM12). The TM8 of ABCA3 unwinds near the luminal membrane surface to form a short α helix TM8a, and the last exocytosolic loop of ABCA3 contains a short α helix EH5 in addition to the V-shaped α-helical hairpins EH3-EH4 (fig. S7D). In this lateral-opening conformation, the two TMDs contact each other through a narrow interface between TM5 and TM11 near the cytosolic membrane surface, and the other lateral surfaces of the TMDs are completely exposed to the lipid bilayer in both membrane leaflets (Fig. 3A and fig. S7, A to C). Therefore, this unique lateral-opening conformation could theoretically permit the lateral access of lipid substrates to the substrate binding sites in TMDs from both membrane leaflets.

A close examination of the TMDs of ABCA3 reveals that it contains two positively charged cavities in the vicinity of the narrow interface between TM5 and TM11 (fig. S7A). Several lipid-like densities could be resolved within the two cavities (Fig. 3A and fig. S7A). Similar lipid-like densities at similar positively charged cavities have also been documented in the resolved nucleotide-free structures of ABCA1 and ABCA4 (fig. S7, B and C) (*27*–*30*). We could not ascertain the specific identities of the lipid-like densities

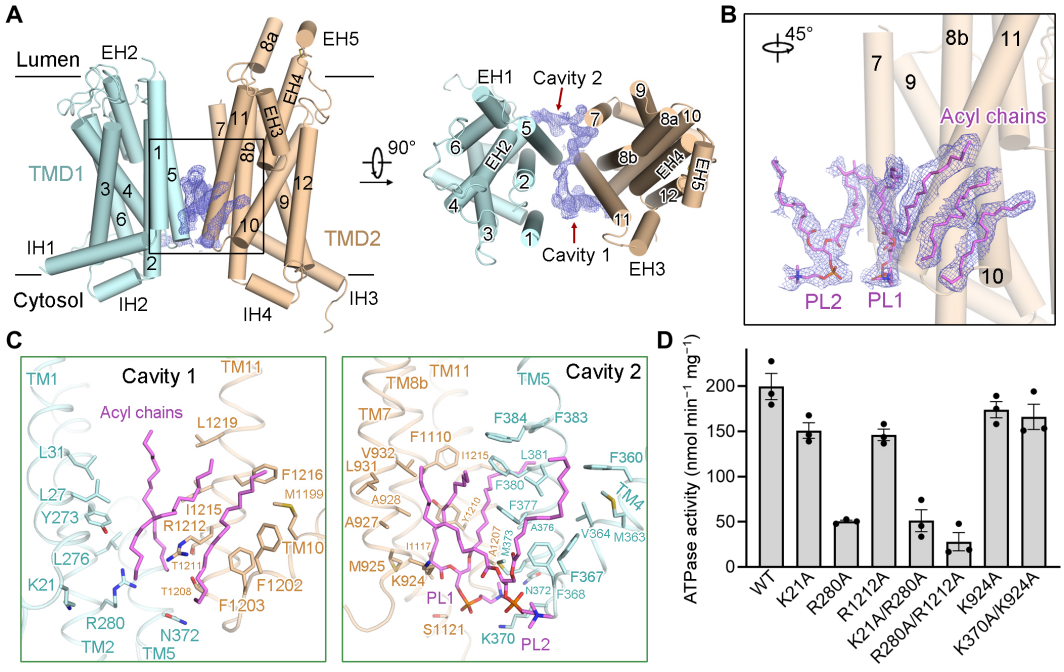

Fig. 3. Two positively charged cavities within the TMDs in the cytosolic membrane leaflet. (**A**) Two perpendicular views of the TMDs of ABCA3. The lipid-like densities, observed in cavities 1 and 2 between the TMDs in the cytosolic membrane leaflet, are shown as blue mesh, contoured at 3σ. (**B**) A close-up view of the lipid-like densities and the superimposed PLs and acyl chains. PLs and acyl chains are shown in purple sticks. (**C**) Close-up views of the lipid-binding sites. Residues involved in lipid coordination in cavities 1 and 2 are shown as sticks. (**D**) Functional characterization of key residues mediating the interactions evaluated by ATPase activity of ABCA3.

within the cavity 1. The densities might result from the acyl chains of phospholipids (PLs), the sterols, or the other lipidic species and were tentatively assigned as three acyl chains in our structure (Fig. 3, A and B, and fig. S8A). Nonetheless, the lipid-like densities within the cavity 2 can be well fitted with two PL molecules (tentatively assigned as PC in our structure) (Fig. 3, A and B, and fig. S8A). Consistent with the observations, PL molecules [mainly PC and phosphatidylethanolamine (PE)] can be detected and confirmed in purified ABCA3 by thin-layer chromatography (TLC) and tandem mass spectrometry (MS) (fig. S8, B and C).

As the two TMDs have a very limited interaction interface in the cytosolic membrane leaflet, the lipid molecules filled in cavities between the two TMDs seem to be important for maintaining the stability of TMD in this lateral-opening conformation (Fig. 3A). We serendipitously found that, when the LMNG and CHS detergent was applied in the whole protein purification procedure, the purified ABCA3 protein behaved well in SEC but showed markedly diminished copurified PLs and displayed nearly abolished ATPase activity (fig. S9, A to C). The cryo-EM analysis of this "delipidated" protein only yielded a low-resolution reconstruction at an overall resolution of 6.3 Å that displayed highly flexible NBDs and RDs (fig. S9, D to F), suggesting the decreased protein stability due to the removal of lipids from the TMDs. Consistent with this, the TMDs of this delipidated ABCA3 exhibited a conformation distinct from the lateral-opening conformation but closed to the ATP-bound conformation discussed in the next section, which precludes the lipid binding to the TMDs (fig. S9G).

Three positively charged residues—Lys^{21}, Arg^{280}, and Arg^{1212}—and three polar residues—Asn^{372}, Thr^{1208}, and Thr^{1211}—could be found near the bottom of cavity 1 in the cytosolic side and might be responsible for the coordination of the polar heads of the lipids; meanwhile, plenty of hydrophobic residues from TMs 1/2/10/11 participate in the coordination of the hydrophobic acyl chains (Fig. 3C and fig. S10A). Two positively charged residues, Lys^{370} and Lys^{924}, and two polar residues, Asn^{372} and Ser^{1121}, which are near the bottom of cavity 2 in the cytosolic side, could help to position the polar heads of PLs; meanwhile, the acyl chains of PLs are within hydrophobic environments created by a great number of hydrophobic residues from TMs 4/5/7/8b/11 (Fig. 3C and fig. S10B). To inspect the importance of lipid binding, we performed mutagenesis studies targeting the positively charged residues within the binding cavities. The K21A, R280A, R1212A, K21A/R280A, and R280A/R1212A variants, designed to disturb the lipid binding to cavity 1, displayed similar protein expression and solution behavior in SEC (fig. S10C). The K21A and R1212A variants displayed approximately 25% reduction in ATPase activity, whereas the R280A, K21A/R280A, and R280A/R1212A variants exhibited approximately 75% reduction in ATPase activity, consistent with the centrally positioned localization of Arg^{280} in cavity 1 (Fig. 3, C and D). The reduction in ATPase activity was likely due to the impaired lipid binding, which led to decreased protein stability. In contrast, the K924A and K370A/K924A variants, conceived to affect the lipid binding to cavity 2, showed similar protein expression and solution behavior in SEC (fig. S10C) and displayed only slightly decreased ATPase activity compared to the WT protein (Fig. 3D). Together, our results suggest that lipid binding to cavity 1 instead of cavity 2 is more important for protein stability and ATPase activity, a phenomenon that has also been noted in ABCA4 (*30*).

Structure of the ATP-bound ABCA3

To trap ABCA3 in the ATP-bound state, we used the E690Q/E1540Q mutant to eliminate the ATP hydrolysis while retaining the ATP binding. The structure of E690Q/E1540Q mutant was determined in the presence of 10 mM ATP-Mg^{2+} to an overall resolution of 3.3 Å (fig. S11). The EM map is of high quality for most of the protein (fig. S11E), permitting the model building of 1566 residues with 1563 side chains assigned (table S1).

In the presence of ATP, ABCA3 adopts a very different conformation compared to that of the nucleotide-free structure (Fig. 4A). As expected, two well-defined ATP-Mg^{2+} molecules can be observed, which were sandwiched between the Walker A motifs and the ABC signature motifs of opposing NBDs (fig. S12, A and B). In the ATP-bound state, the two NBDs of ABCA3 form a classic "head-to-tail" and closed dimer as predicted for all ABC transporters (fig. S12B) (*26*, *40*). The two ATP molecules are bound in highly conserved manners as those in the ATP-bound ABCA4 structure (fig. S12C). Except the ECDs, the TMDs, NBDs, and RDs of ABCA3 in the ATP-bound state share almost identical conformations as those of the ATP-bound ABCA4 structure (fig. S13).

Conserved conformational changes of ABCA3 upon binding of ATP

Although ABCA3 and ABCA4 are supposed to transport the lipid substrates in opposite directions, they share conserved conformational changes upon binding of ATP, shifting from a lateral-opening conformation to a closed conformation (Fig. 4B). In the ATP-bound state, the gaps between the two TMDs in both membrane leaflets are completely collapsed, giving no space for substrate binding (Fig. 4B). The ATP-bound state might represent a state after substrate release but preceding ATP hydrolysis. The two TMDs form intensive interactions between TMs 1/2/5 and TMs 7/8b/11, which may stabilize the closed conformation of TMDs (Fig. 4B).

Upon ATP binding, the cytosolic domains undergo several local conformational changes. The RecA-like domains of the NBDs and the RDs rotate by around 30° relative to the α-helical domains of NBDs (fig. S12, D and E). Aside from these local conformational changes, the motions of the two TMD-NBD-RD modules between these two states can be largely described as rigid-body movements, because the two modules remain roughly unchanged in the two different states (Fig. 4, C and D). However, both ECDs show evident rotations relative to the corresponding TMD-NBD-RD modules upon binding of ATP (Fig. 4, C and D). The four connecting loops (CLs) between ECDs and TMDs (named CL1 to CL4) undergo approximately 7 to 14 Å movements upon ATP binding, which translates to a roughly 30 Å displacement observed at the outside of the ECDs (Fig. 4, C and D). In the ATP-bound state, the TM8a unwinds into a loop, accompanied with the movement of ECD2 (Fig. 4D). Because the entire ECD is virtually identical in both states (RMSD = 0.529 Å), except for some apparent local conformational changes for the CL3 and CL4 (Fig. 4E), the altered conformation of ABCA3-ECD can be described as rigid-body rotations between the two states, similar to the observed conformational change of ABCA4-ECD upon ATP binding (*30*).

Structural interpretation of the disease-associated mutations

Before our study, several attempts have been applied to the computational 3D structural modeling of human ABCA3 to understand the possible impact of pathogenic variants (*41*–*43*). These computational 3D models were built on the basis of the type IV ABC fold (*41*), the TMDs-NBDs of nucleotide-free ABCA1 structure (*42*), and the TMDs-NBDs-RDs of ATP-bound ABCA4 structure (*43*), respectively, and thus provide inaccurate and limited interpretation of ABCA3 variants. The high-resolution structures of ABCA3 in both nucleotide-free and ATP-bound states presented here could provide direct insights into the mechanistic basis for the pathogenic mutations. Among the missense mutations targeting 101 residues in human ABCA3 (Human Gene Mutations Database, www.hgmd.cf.ac.uk), which are associated with various lung diseases, 97 residues can be reliably mapped to both ABCA3 structures (Fig. 5A and table S2). These pathogenic missense variants spread over the entire ABCA3 structure, suggesting the functional importance of all the structural domains.

Our structures offer the opportunity to evaluate the specific impact of individual ABCA3 missense mutations, and we will take three representative mutations as examples for analyses. The hydrophobic residues Leu^{101} in ECD1 and Leu^{982} in ECD2 are buried within the hydrophobic core of these domains (Fig. 5B). Replacement of these two residues by proline (L101P or L982P variant) would likely cause protein-folding defects, which is consistent with the reported misfolding and abnormal intracellular localization of both variants (defined as type I mutations) (*44*–*46*). The most frequent ABCA3 missense variant in humans, E292V (*47*), is positioned within the coupling helix IH2 of TMD1 (Fig. 5C), located distal to the ATP hydrolysis site, and might be involved in the interdomain coupling between TMD1 and NBD1 during the catalytic cycle. The Glu^{292} is a surface-exposed residue that makes salt bridges with the other residues in NBD1 in both nucleotide-free and ATP-bound states (Fig. 5C). The E292V variant should not affect the protein folding, thus could be trafficked to normal intracellular sites (*48*, *49*). However, it might slightly impair the coupling between TMD1 and NBD1, resulting in moderate decrease of ATP hydrolysis and partially reduced lipid transport (defined as type II mutation) (*48*, *49*). Apart from mechanistic insights of the currently described disease-causing mutations in ABCA3, our structures could also be implicated in related therapeutic studies in the future.

DISCUSSION

Human ABCA3 is involved in the export of surfactant lipids—such as PC, PG, and cholesterol—from the cytosol into the intracellular vesicles (*8*, *11*–*14*). The two positively charged cavities within the cytosolic membrane leaflet of TMDs and the lipid-like densities observed within the two cavities strongly suggest that these two cavities are most likely the substrate binding sites, responsible for the export of surfactant lipid across the limiting membrane of LBs. Although cavity 1 instead of cavity 2 is supposed to be more important for protein stability and ATPase activity, we could not tell which one or whether both are the real substrate binding sites without lipid transport assay. The structure of ABCA3 in the ATP-bound state represents the ATP-bound structure of exporters in the ABCA subfamily. The structures of ABCA3 in two distinct functional states presented here suggest a model for the ABCA3-mediated lipid export (Fig. 6A). In the nucleotide-free state, the TMDs of ABCA3 display a lateral-opening conformation, allowing the lateral access of lipid substrates from the cytosolic membrane leaflet to the substrate binding sites within the TMDs (Fig. 6A, left). Upon binding of ATP, ABCA3 undergoes large conformational changes in TMDs, ECDs, and RDs accompanied with ATP-induced NBD closure. The two TMDs convert

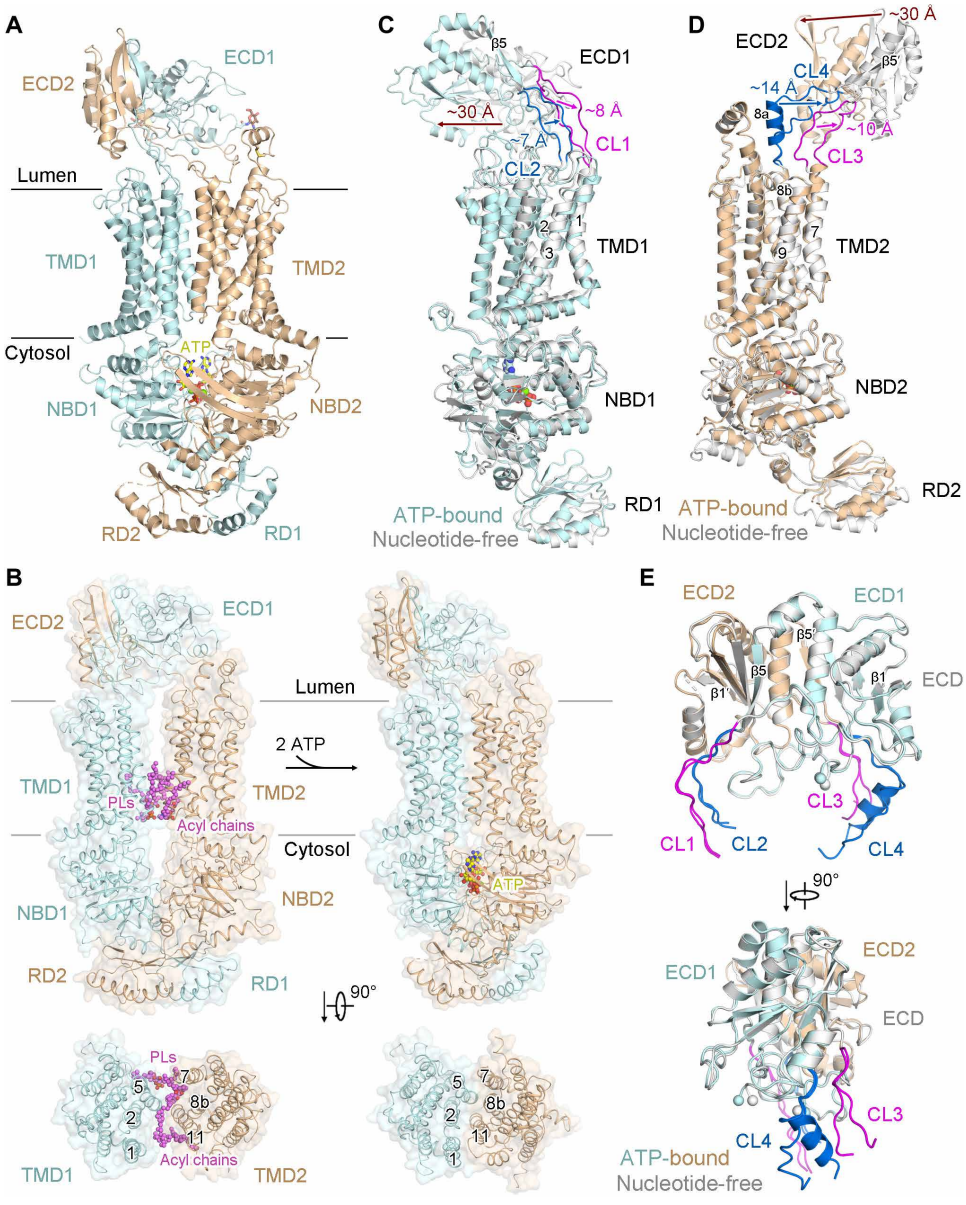

Fig. 4. Conformational changes of ABCA3 upon ATP binding. (**A**) Overall structure of ATP-bound ABCA3. The domains are colored as above. (**B**) Closure of the ABCA3 TMDs and NBDs upon ATP binding. PLs and acyl chains are shown as purple spheres. ATP and Mg^{2+} are displayed as yellow and green spheres, respectively. (**C**) Superposition of half 1 of the nucleotide-free ABCA3 (gray) and ATP-bound ABCA3 (light cyan) structures. The connecting loops between TMD1 and ECD1, abbreviated as CL1 and CL2, are colored magenta and marine, respectively. The CL1 and CL2 in the ATP-bound structure exhibit ~8 and ~7 Å displacements, respectively, compared to those in the nucleotide-free structure. The ECD1 rotates forward with a movement of ~30 Å observed at the outside. (**D**) Superposition of half 2 of the nucleotide-free ABCA3 (gray) and ATP-bound ABCA3 (wheat) structures. The connecting loops between TMD2 and ECD2, abbreviated as CL3 and CL4, are colored magenta and marine, respectively. TM8a of CL4 was unwound in the ATP-bound structure. The CL3 and CL4 in the ATP-bound structure exhibit ~10 and ~14 Å displacements, respectively, compared to those in the nucleotide-free structure. The ECD2 rotates backward with a movement of ~30 Å observed at the outside. (**E**) Superposition of ECD of the nucleotide-free ABCA3 (gray) and ATP-bound ABCA3 (light cyan and wheat) structures. CL1 and CL3 are colored magenta; CL2 and CL4 are colored marine.

to a closed conformation with collapsed substrate binding sites and extrude the lipid substrates across the membranes (Fig. 6A, right). ATP hydrolysis then resets ABCA3 to the nucleotide-free state in lateral-opening conformation ready for next transport cycle.

Although ABCA3 and ABCA4 transport the lipid substrates in opposite directions, they adopt highly conserved ATP-driven conformational changes, named as lateral access and extrusion (*30*), to "flop" or "flip" the lipid substrates across the membranes (Fig. 6, A and B). Our study not only suggests that the two positively charged cavities within the TMDs of ABCA3 are the potential lipid substrate binding sites but also reveals that the lipids bound inside the cavity 1 are critical for protein stability and activity and are essential to maintain the TMDs of nucleotide-free ABCA3 in a lateral-opening conformation (fig. S9). In the TMDs of ABCA4, the physiological lipid substrate *N*-retinylidene-phosphatidylethanolamine (NRPE) locates in the luminal membrane leaflet and is primarily sandwiched between

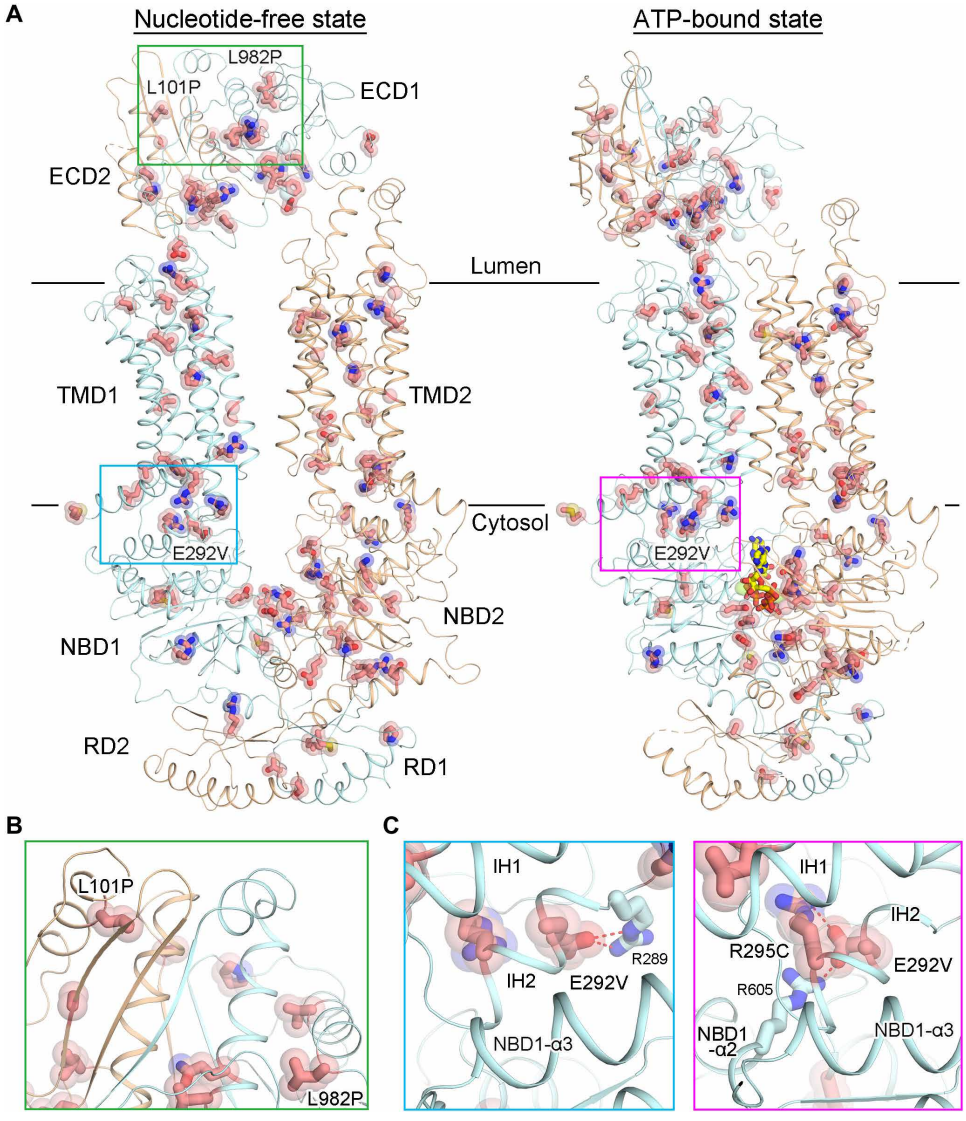

Fig. 5. Structural mapping of the pathogenic mutations. (**A**) Mapping the locations of disease-associated missense mutations using the nucleotide-free and the ATP-bound structures of ABCA3. (**B**) Two missense mutations, L101P and L982P, were buried within the hydrophobic core of ECD, suggesting that they would likely cause protein-folding defects. This type of mutation was defined as type I mutation. (**C**) The most frequent missense mutation, E292V, is positioned within the coupling helix IH2 of TMD1. The potential polar interactions between Glu^{292} and neighboring residues are shown as red dashed lines. The E292V variant would not affect the protein folding but slightly impair the coupling between TMD1 and NBD1, resulting in moderate functional impairment in ATP hydrolysis. This type of mutation was defined as type II mutation.

the two TMDs and further coordinated by an extended loop from ECD1 (Fig. 6B and fig. S7B). Aside from the NRPE substrate, some lipid molecules were also observed within the TMDs of ABCA4 in the cytosolic membrane leaflet in all the resolved nucleotide-free ABCA4 structures (*28*–*30*). These lipids might not be the substrates for transport but serve as structural roles for stabilizing the protein in a lateral-opening conformation (Fig. 6B). However, how the lipid substrates can be flopped or flipped across the membranes through conserved ATP-driven conformational changes and the molecular determinants for the opposite substrate transport directionality of ABCA3 and ABCA4 remains to be explored in the future. Furthermore, the pathways for substrate translocation also await characterization.

The TMDs of ABCA3/ABCA4/ABCA1 share a common lateral-opening conformation in the nucleotide-free state but exhibit some differences in the substrate binding sites. For instance, the NRPE substrate binding site in ABCA4 does not exist in ABCA3 or ABCA1. In addition, the lipid-like densities accommodated in their positively charged cavities within the cytosolic membrane leaflet of TMDs, and the corresponding coordinating residues within the cavities also display a certain degree of variations (fig. S7). The dissimilarity might be the reason for or result of the different substrate selectivity of ABCA transporters. It has been demonstrated that ABCA1 and ABCA7 could preferentially transport PC, phosphatidylserine, and sphingomyelin, whereas ABCA4 would preferentially transport PE and NRPE (*34*, *35*). Additional biochemical and structural

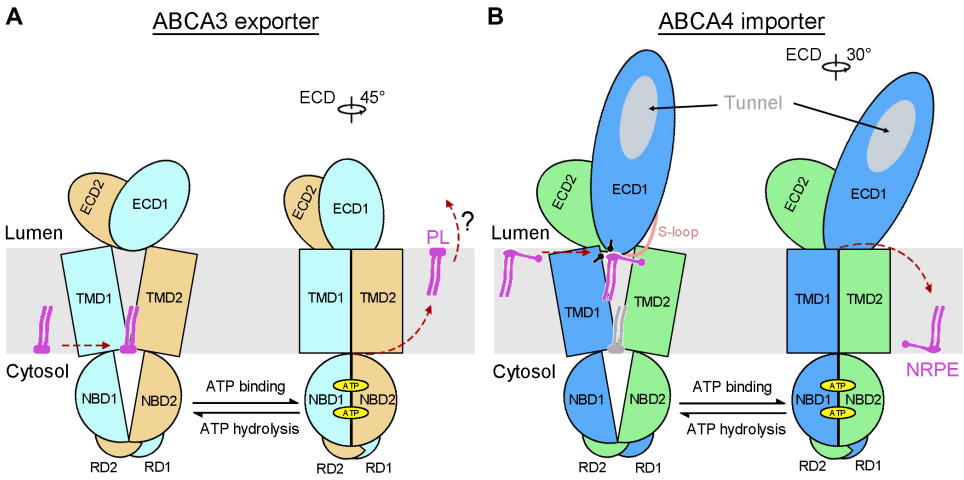

Fig. 6. Working models of the ABCA transporters. Schematic diagram of the lateral access and extrusion cycle of the ABCA3 exporter (**A**) and the ABCA4 importer (**B**). The ABCA exporters and importer might exhibit similar working mechanisms. In the absence of ATP, the TMDs display a V-shaped lateral-opening conformation, allowing the lateral access of the lipid substrates (magenta, shown as PL in the case of exporters and NRPE in the case of importer) from either the cytosolic leaflet (in the case of exporters) or the luminal leaflet (in the case of importer) of the membrane. ATP binding triggers the closure of TMDs, which might lead to the extrusion of the substrates to the other leaflet of the membrane. The hydrolysis of ATP resets the ABCA transporters to the lateral-opening conformation ready for the next transport cycle. How the PL flopped by ABCA3 can enter and be stored in LBs requires further investigation. A PL molecule (gray) bound to the TMDs of nucleotide-free ABCA4 in the cytosolic membrane leaflet was also presented in the model. It might be responsible for maintaining the protein stability of nucleotide-free ABCA4.

studies are necessitated to resolve the substrate selectivity of ABCA3 and the specific residues that confer differences in substrate selectivity between the ABCA subfamily transporters.

The structures of ABCA3, lacking the lipid storage or delivery tunnel and the lid in the ECD, represent the structures of ABCA transporters with smaller ECDs. The ECDs of ABCA3/5/6/8/9/10 are about ~170 to 180 amino acids and ~140 to 150 amino acids in length for ECD1 and ECD2, respectively, whereas the ECDs of ABCA1/2/4/7/12/13 are more than 500 amino acids and more than 210 amino acids in length for ECD1 and ECD2, respectively (*19*). The sequences and lengths of ECDs are highly conserved among the ABCA3/5/6/8/9/10 transporters (fig. S14), suggesting a preserved architecture for these smaller ABCA transporters. Because of the lack of lipid storage or delivery tunnel in ABCA3-ECD, further studies would be required to investigate how the lipid flopped by ABCA3 can enter and be stored in the LBs (Fig. 6A). A recent study has suggested that the surfactant protein B (SP-B) inside the LBs might be able to extract the surfactant lipids flopped by ABCA3 (*50*), a function similar to that of the lipid storage or delivery tunnel in larger ABCA transporters. Whether the SP-B could fulfill the function of the tunnels and whether other downstream lipid acceptor proteins exist for other smaller ABCA transporters require further explorations.

The proteolytic cleavage in the ECD1 of ABCA3 has not been reported in any other ABCA or even ABC transporters. Our results reveal that this cleavage would yield two closely interacting fragments (a small NTF and a large CTF) of ABCA3, although this cleavage would not affect its ATPase activity (Fig. 1, D to G). Further studies are required to ascertain whether this cleavage could influence the functions of ABCA3 in other aspects except the ATPase activity, such as the lipid transport activity or its interaction with upstream/downstream factors.

Despite many remaining questions, the biochemical and structural studies of human ABCA3 represent a major step toward the mechanistic understanding of ABCA3-mediated lipid export. The work establishes a new starting point to understand the molecular basis of the ABCA3-related lung diseases and may facilitate the structure-based drug design targeting ABCA3. The structural analysis suggests a conserved lateral access and extrusion paradigm for both lipid export and import mediated by ABCA transporters. This working model is distinct from the conventional "alternating-access" model for most transporters (*26*, *51*) and the "credit card swipe" model for the other lipid transporters (*52*, *53*) and could serve as an important framework for future studies toward other ABCA subfamily transporters.

MATERIALS AND METHODS

Protein expression and purification

The human ABCA3 WT and variants were cloned into the pCAG vector and fused with an N-terminal Flag tag and a C-terminal His_{10} tag. The HEK293F suspension cells (Invitrogen) were cultured at 37°C under 5% CO_2 in SMM 293-TII medium (Sino Biological Inc.). Each liter of cells was transiently transfected with preincubated 1 mg of plasmid and 3 mg of polyethyleneimine (Polysciences) at a density of 2.0 × 10^6 to 2.5 × 10^6 cells/ml. About 10 mM sodium butyrate was added into the culture to increase protein expression after infection for 12 hours. The cells were cultured for another 48 hours. before being harvested.

The cell pellet was resuspended in lysis buffer [25 mM tris (pH 7.5) and 150 mM NaCl] supplemented with protease inhibitor cocktail (AMRESCO). The membrane protein was extracted with 1% (w/v) LMNG and 0.2% (w/v) CHS at 4°C for 2 hours. After centrifugation at 37,000*g* for 1 hour, the supernatant was collected and applied to anti-Flag G1 affinity resin (GenScript), rinsed with W1 buffer [25 mM tris (pH 7.5), 150 mM NaCl, and 0.02% GDN]. The resin was washed with 20 column volumes of W1 buffer before being eluted with W1 buffer supplemented with Flag peptide (200 μg/ml). The protein was further purified by nickel affinity chromatography.

The Ni–nitrilotriacetic acid resin (QIAGEN) was washed with W2 buffer [25 mM tris (pH 7.5), 150 mM NaCl, 20 mM imidazole, and 0.02% GDN] and eluted with W2 buffer supplemented with 230 mM imidazole. The concentrated protein eluent was further purified by SEC using a Superose 6 Increase 10/300 GL column (GE Healthcare) equilibrated with W1 buffer. Peak fractions were collected and concentrated for activity assay or cryo-EM experiments. ABCA3 protein purified in LMNG/CHS was prepared similarly, except that 0.02% GDN was replaced with 0.02% LMNG and 0.004% CHS.

ATPase activity assay

The ATPase activity of ABCA3 was measured similarly as that of ABCA4 by a continuous spectrophotometric assay based on the coupling of adenosine 5′-diphosphate production and NADH (reduced form of nicotinamide adenine dinucleotide phosphate) oxidation by pyruvate kinase (PK) and lactate dehydrogenase (LDH) (*30*, *54*). The assay was performed at 37°C on a 150-μl scale in 96-well plates. The reaction mixture included 25 mM tris (pH 7.5), 150 mM NaCl, 0.02% GDN, PK (60 μg/ml), LDH (32 μg/ml), 3 mM phosphoenolpyruvate, 0.4 mM NADH, 0.1 μM ABCA3, and varying amounts of ATP/$MgCl_2$. Measurements was recorded at 340 nm, monitoring the decrease of NADH absorbance over the course of 1 hour on Synergy H1 microplate reader (BioTek). Statistical analysis was carried out with GraphPad Prism 8. The ATP hydrolysis rate versus ATP concentration was fitted with the Michaelis-Menten equation.

Protein deglycosylation and Western blot analysis

About 1 μg of ABCA3 protein was denatured and treated with 0.3 μl of PNGase F (P0708S, New England Biolabs) in 20 μl of reaction mixture at 37°C for 1 hour before being applied to SDS-PAGE and transferred to polyvinylidene difluoride membranes (Millipore). After blocking with 5% milk [in PBST, phosphate-buffered saline (PBS) with 0.1% Tween 20] at room temperature (RT) for 1 hour, the membranes were incubated with primary mouse anti-Flag (D191041, Sangon Biotech) or mouse anti-His (D191001, Sangon Biotech) monoclonal antibodies (1:5000 dilution in PBST) at RT for 2 hours. Following three rounds of 5-min wash in PBST, the membranes were incubated with horseradish peroxidase–conjugated goat anti-mouse immunoglobulin G antibodies (1:7000 dilution in PBST; D110087, Sangon Biotech) at RT for 1 hour and developed with UltraSignal hypersensitive ECL chemiluminescence substrate (4AW011, 4A Biotech) on an Amersham Imager 600 (GE Healthcare).

TLC and MS analysis

Both TLC and liquid chromatography (LC)–MS/MS was performed similarly as that for ABCA4 (*30*). For TLC, chloroform and methanol were mixed with 1 ml of ABCA3 (0.2 mg in total) with a volume ratio of 0.5:1:1 for lipid extraction. The mixture was sonicated for 30 min in ice water bath before being spun at 2300*g* for 10 min at 4°C. The chloroform phase at bottom was collected and dried under a nitrogen stream. The lipids were dissolved in 20 μl of chloroform, and about 5 μl of sample was applied onto a silica TLC plate (100 mm by 100 mm; Qingdao Ocean Chemicals). The lipids were separated by a solvent system containing chloroform, methanol, and water [65:25:4 (v/v/v)] for 30 min. The TLC plate was dried and stained with iodine vapor for overnight to visualize the lipids.

For LC-MS/MS, the lipids were extracted similarly as above and resuspended in 20 μl of Acetonitrile (ACN)/Isopropyl alcohol (IPA)/H_2O [65:30:5 (v/v/v)] solution containing 5 mM ammonium acetate. About 5 μl of sample was injected into the LC-MS/MS system (Q Exactive Orbitrap mass spectrometer, Thermo Fisher Scientific) equipped with a C18 reversed-phase column (1.9 μm, 2.1 mm by 100 mm; Thermo Fisher Scientific). Mobile phase A was ACN/H_2O [60:40 (v/v)] with 10 mM ammonium acetate, and mobile phase B was IPA/ACN [90:10 (v/v)] with 10 mM ammonium acetate. The elution gradient, started with 32% mobile phase B for 1.5 min, was linearly increased to 85% mobile phase B at 15.5 min. Then, the gradient was raised to 97% mobile phase B at 15.6 min and held until 18 min. Last, the gradient was decreased to 32% mobile phase B at 18.1 min for column equilibration until 22 min. The flow rate was 0.26 ml/min. The mass spectrometer was operated in negative mode with a spray voltage of 3.5 kV. Full-scan MS data were obtained from the mass/charge ratio (m/z) range of 166.7 to 2000. The MS/MS spectra were searched against the lipid database using the LipidSearch software (Thermo Fisher Scientific). The peaks for PL ions, with retention time between 9.5 and 14.0 min, from m/z range of 670 to 850 were indicated.

Cryo-EM sample preparation and data collection

For cryo-EM sample preparation of nucleotide-free ABCA3, 3-μl aliquots of purified WT ABCA3 (~10 mg/ml) were applied to the glow-discharged QUANTIFOIL Cu R1.2/1.3 300 mesh grids. After being blotted for 4.5 s at 8°C with 100% humidity, the grids were flash-frozen in liquid ethane cooled by liquid nitrogen with Vitrobot (Mark IV, Thermo Fisher Scientific). For the ATP-bound ABCA3 sample, ABCA3 (~10 mg/ml) (E690Q/E1540Q) was incubated with 10 mM ATP/$MgCl_2$ on ice for 1 hour before grid preparation.

For nucleotide-free ABCA3 sample purified in GDN, a total of 1808 movie stacks were collected with SerialEM (*55*) on a Titan Krios microscope with a K2 Summit direct electron detector (Gatan) and a GIF Quantum energy filter (Gatan) with a slit width of 20 eV at a nominal magnification of ×130,000 with defocus values between −2.0 and − 1.0 μm. Each stack was exposed in superresolution mode for 5.76 s in 32 frames. The total dose for each stack was 50 $e^-/Å^2$. For nucleotide-free ABCA3 sample purified in LMNG/CHS and ATP-bound ABCA3 sample, 3253 movie stacks and 938 movie stacks were individually collected in the same manner. All the stacks were motion-corrected using MotionCor2 (*56*) with a binning factor of 2, resulting in a pixel size of 1.08 Å; meanwhile, dose weighting was performed (*57*). The defocus values were estimated by Gctf (*58*).

Cryo-EM data processing

For the dataset of nucleotide-free ABCA3 in GDN, a total of 1,218,288 particles were picked from 1808 micrographs using Relion 3.0 (*59*). After 2D classification, 988,000 particles were selected and subjected to global search 3D classification. A total of 637,131 particles selected from the global search 3D classification were subjected to 3D autorefinement. After another round of local search 3D classification, a total of 111,435 particles were selected. 3D autorefinement of the particles with an adapted mask yielded a map with an overall resolution of 3.3 Å.

The procedures for LMNG/CHS-purified ABCA3 and ATP-bound ABCA3 data processing were similar as above. For the dataset of nucleotide-free ABCA3 in LMNG/CHS, 2,179,653 particles were picked from 3253 micrographs. 2D classification resulted in 1,043,293 particles that were then subjected to global search 3D classification. After further 3D classification without alignment bearing an adapted mask, a total of 153,740 particles were selected. 3D autorefinement

of the particles with mask yielded a 6.3 Å reconstruction. For the ATP-bound ABCA3 dataset, a total of 490,349 particles were picked from 938 micrographs. 2D classification resulted in 398,321 good particles that were then subjected to global search 3D classification. After an additional round of local search 3D classification, a total of 80,575 particles were selected. 3D autorefinement of the particles with an adapted mask yielded a reconstruction at resolution of 3.3 Å.

All 2D classification, 3D classification, and 3D autorefinement procedures were performed using Relion 3.0. Resolutions were estimated using the gold-standard Fourier shell correlation 0.143 criterion (*60*) with high-resolution noise substitution (*61*).

Model building and refinement

The human apo ABCA4 model (PDB code 7E7I) was used as the initial reference for model building of nucleotide-free ABCA3 purified in GDN. The ABCA4 subdomains (TMDs, NBDs, RDs, and ECD base) were individually docked into the 3.3 Å map of nucleotide-free ABCA3 using Chimera (*62*). Each residue was mutated and manually adjusted with Coot (*63*). Structure refinements were carried out by Phenix (1.18.1_3865) (*64*) in real space with secondary structure and geometry restraints. The structural model was validated by Phenix and MolProbity (*65*). The nucleotide-free ABCA3 structure was used as the reference for model building of ATP-bound ABCA3. The model refinement and validation statistics were summarized in table S1.

SUPPLEMENTARY MATERIALS

Supplementary material for this article is available at https://science.org/doi/10.1126/sciadv.abn3727

View/request a protocol for this paper from *Bio-protocol*.

REFERENCES AND NOTES

1. J. R. Wright, L. G. Dobbs, Regulation of pulmonary surfactant secretion and clearance. *Annu. Rev. Physiol.* **53**, 395–414 (1991).
2. S. A. Rooney, S. L. Young, C. R. Mendelson, Molecular and cellular processing of lung surfactant. *FASEB J.* **8**, 957–967 (1994).
3. M. Griese, Pulmonary surfactant in health and human lung diseases: State of the art. *Eur. Respir. J.* **13**, 1455–1476 (1999).
4. U. S. Ryan, J. W. Ryan, D. S. Smith, Alveolar type II cells: Studies on the mode of release of lamellar bodies. *Tissue Cell* **7**, 587–599 (1975).
5. J. J. Batenburg, Surfactant phospholipids: Synthesis and storage. *Am. J. Physiol.* **262**, L367–L385 (1992).
6. G. Yamano, H. Funahashi, O. Kawanami, L. X. Zhao, N. Ban, Y. Uchida, T. Morohoshi, J. Ogawa, S. Shioda, N. Inagaki, ABCA3 is a lamellar body membrane protein in human lung alveolar type II cells. *FEBS Lett.* **508**, 221–225 (2001).
7. S. Mulugeta, J. M. Gray, K. L. Notarfrancesco, L. W. Gonzales, M. Koval, S. I. Feinstein, P. L. Ballard, A. B. Fisher, H. Shuman, Identification of LBM180, a lamellar body limiting membrane protein of alveolar type II cells, as the ABC transporter protein ABCA3. *J. Biol. Chem.* **277**, 22147–22155 (2002).
8. Y. Matsumura, H. Sakai, M. Sasaki, N. Ban, N. Inagaki, ABCA3-mediated choline-phospholipids uptake into intracellular vesicles in A549 cells. *FEBS Lett.* **581**, 3139–3144 (2007).
9. N. Ban, Y. Matsumura, H. Sakai, Y. Takanezawa, M. Sasaki, H. Arai, N. Inagaki, ABCA3 as a lipid transporter in pulmonary surfactant biogenesis. *J. Biol. Chem.* **282**, 9628–9634 (2007).
10. N. Cheong, H. Zhang, M. Madesh, M. Zhao, K. Yu, C. Dodia, A. B. Fisher, R. C. Savani, H. Shuman, ABCA3 is critical for lamellar body biogenesis in vivo. *J. Biol. Chem.* **282**, 23811–23817 (2007).
11. M. L. Fitzgerald, R. Xavier, K. J. Haley, R. Welti, J. L. Goss, C. E. Brown, D. Z. Zhuang, S. A. Bell, N. Lu, M. Mckee, B. Seed, M. W. Freeman, ABCA3 inactivation in mice causes respiratory failure, loss of pulmonary surfactant, and depletion of lung phosphatidylglycerol. *J. Lipid Res.* **48**, 621–632 (2007).
12. R. Zarbock, E. Kaltenborn, S. Frixel, T. Wittmann, G. Liebisch, G. Schmitz, M. Griese, ABCA3 protects alveolar epithelial cells against free cholesterol induced cell death. *Biochim. Biophys. Acta* **1851**, 987–995 (2015).
13. S. Höppner, S. Kinting, A. A. Torrano, U. Schindlbeck, C. Bräuchle, R. Zarbock, T. Wittmann, M. Griese, Quantification of volume and lipid filling of intracellular vesicles carrying the ABCA3 transporter. *Biochim. Biophys. Acta Mol. Cell Res.* **1864**, 2330–2335 (2017).
14. Y. Li, S. Kinting, S. Höppner, M. E. Forstner, O. Uhl, B. Koletzko, M. Griese, Metabolic labelling of choline phospholipids probes ABCA3 transport in lamellar bodies. *Biochim. Biophys. Acta Mol. Cell Biol. Lipids* **1864**, 158516 (2019).
15. S. Shulenin, L. M. Nogee, T. Annilo, S. E. Wert, J. A. Whitsett, M. Dean, *ABCA3* gene mutations in newborns with fatal surfactant deficiency. *N. Engl. J. Med.* **350**, 1296–1303 (2004).
16. J. E. Bullard, S. E. Wert, J. A. Whitsett, M. Dean, L. M. Nogee, ABCA3 mutations associated with pediatric interstitial lung disease. *Am. J. Respir. Crit. Care Med.* **172**, 1026–1031 (2005).
17. F. Flamein, L. Riffault, C. Muselet-Charlier, J. Pernelle, D. Feldmann, L. Jonard, A. M. Durand-Schneider, A. Coulomb, M. Maurice, L. M. Nogee, N. Inagaki, S. Amselem, J. C. Dubus, V. Rigourd, F. Brémont, C. Marguet, J. Brouard, J. de Blic, A. Clement, R. Epaud, L. Guillot, Molecular and cellular characteristics of ABCA3 mutations associated with diffuse parenchymal lung diseases in children. *Hum. Mol. Genet.* **21**, 765–775 (2012).
18. N. Klugbauer, F. Hofmann, Primary structure of a novel ABC transporter with a chromosomal localization on the band encoding the multidrug resistance-associated protein. *FEBS Lett.* **391**, 61–65 (1996).
19. F. Peelman, C. Labeur, B. Vanloo, S. Roosbeek, C. Devaud, N. Duverger, P. Denèfle, M. Rosier, J. Vandekerckhove, M. Rosseneu, Characterization of the ABCA transporter subfamily: Identification of prokaryotic and eukaryotic members, phylogeny and topology. *J. Mol. Biol.* **325**, 259–274 (2003).
20. W. E. Kaminski, A. Piehler, J. J. Wenzel, ABC A-subfamily transporters: Structure, function and disease. *Biochim. Biophys. Acta* **1762**, 510–524 (2006).
21. J. J. Wenzel, A. Piehler, W. E. Kaminski, ABC A-subclass proteins: Gatekeepers of cellular phospho- and sphingolipid transport. *Front. Biosci.* **12**, 3177–3193 (2007).
22. C. Albrecht, E. Viturro, The ABCA subfamily—Gene and protein structures, functions and associated hereditary diseases. *Pflugers Arch.* **453**, 581–589 (2007).
23. M. Pasello, A. M. Giudice, K. Scotlandi, The ABC subfamily A transporters: Multifaceted players with incipient potentialities in cancer. *Semin. Cancer Biol.* **60**, 57–71 (2020).
24. C. Thomas, R. Tampé, Multifaceted structures and mechanisms of ABC transport systems in health and disease. *Curr. Opin. Struct. Biol.* **51**, 116–128 (2018).
25. C. Thomas, S. G. Aller, K. Beis, E. P. Carpenter, G. Chang, L. Chen, E. Dassa, M. Dean, F. Duong van Hoa, D. Ekiert, R. Ford, R. Gaudet, X. Gong, I. B. Holland, Y. Huang, D. K. Kahne, H. Kato, V. Koronakis, C. M. Koth, Y. Lee, O. Lewinson, R. Lill, E. Martinoia, S. Murakami, H. W. Pinkett, B. Poolman, D. Rosenbaum, B. Sarkadi, L. Schmitt, E. Schneider, Y. Shi, S. L. Shyng, D. J. Slotboom, E. Tajkhorshid, D. P. Tieleman, K. Ueda, A. Váradi, P. C. Wen, N. Yan, P. Zhang, H. Zheng, J. Zimmer, R. Tampé, Structural and functional diversity calls for a new classification of ABC transporters. *FEBS Lett.* **594**, 3767–3775 (2020).
26. C. Thomas, R. Tampé, Structural and mechanistic Principles of ABC transporters. *Annu. Rev. Biochem.* **89**, 605–636 (2020).
27. H. Qian, X. Zhao, P. Cao, J. Lei, N. Yan, X. Gong, Structure of the human lipid exporter ABCA1. *Cell* **169**, 1228–1239.e10 (2017).
28. F. Liu, J. Lee, J. Chen, Molecular structures of the eukaryotic retinal importer ABCA4. *eLife* **10**, e63524 (2021).
29. J. F. Scortecci, L. L. Molday, S. B. Curtis, F. A. Garces, P. Panwar, F. van Petegem, R. S. Molday, Cryo-EM structures of the ABCA4 importer reveal mechanisms underlying substrate binding and Stargardt disease. *Nat. Commun.* **12**, 5902 (2021).
30. T. Xie, Z. Zhang, Q. Fang, B. Du, X. Gong, Structural basis of substrate recognition and translocation by human ABCA4. *Nat. Commun.* **12**, 3853 (2021).
31. L. T. My Le, J. R. Thompson, T. Aikawa, T. Kanikeyo, A. Alam, Cryo-EM structure of lipid embedded human ABCA7 at 3.6Å resolution. bioRxiv 433448 (2021).
32. S. Engelbrecht, E. Kaltenborn, M. Griese, S. Kern, The surfactant lipid transporter ABCA3 is N-terminally cleaved inside LAMP3-positive vesicles. *FEBS Lett.* **584**, 4306–4312 (2010).
33. N. Hofmann, D. Galetskiy, D. Rauch, T. Wittmann, A. Marquardt, M. Griese, R. Zarbock, Analysis of the proteolytic processing of ABCA3: Identification of cleavage site and involved proteases. *PLOS ONE* **11**, e0152594 (2016).
34. F. Quazi, R. S. Molday, Differential phospholipid substrates and directional transport by ATP-binding cassette proteins ABCA1, ABCA7, and ABCA4 and disease-causing mutants. *J. Biol. Chem.* **288**, 34414–34426 (2013).
35. F. Quazi, S. Lenevich, R. S. Molday, ABCA4 is an N-retinylidene-phosphatidylethanolamine and phosphatidylethanolamine importer. *Nat. Commun.* **3**, 925 (2012).
36. M. F. Beers, M. Zhao, Y. Tomer, S. J. Russo, P. Zhang, L. W. Gonzales, S. H. Guttentag, S. Mulugeta, Disruption of N-linked glycosylation promotes proteasomal degradation of the human ATP-binding cassette transporter ABCA3. *Am. J. Physiol. Lung Cell. Mol. Physiol.* **305**, L970–L980 (2013).
37. G. A. Grant, The ACT domain: A small molecule binding domain and its role as a common regulatory element. *J. Biol. Chem.* **281**, 33825–33829 (2006).
38. J.-Y. Lee, L. N. Kinch, D. M. Borek, J. Wang, J. Wang, I. L. Urbatsch, X.-S. Xie, N. V. Grishin, J. C. Cohen, Z. Otwinowski, H. H. Hobbs, D. M. Rosenbaum, Crystal structure of the human sterol transporter ABCG5/ABCG8. *Nature* **533**, 561–564 (2016).

39. N. M. I. Taylor, I. Manolaridis, S. M. Jackson, J. Kowal, H. Stahlberg, K. P. Locher, Structure of the human multidrug transporter ABCG2. *Nature* **546**, 504–509 (2017).
40. D. C. Rees, E. Johnson, O. Lewinson, ABC transporters: The power to change. *Nat. Rev. Mol. Cell Biol.* **10**, 218–227 (2009).
41. A. Paolini, A. Baldassarre, I. Del Gaudio, A. Masotti, Structural features of the ATP-Binding Cassette (ABC) transporter ABCA3. *Int. J. Mol. Sci.* **16**, 19631–19644 (2015).
42. S. Kinting, Y. Li, M. Forstner, F. Delhommel, M. Sattler, M. Griese, Potentiation of ABCA3 lipid transport function by ivacaftor and genistein. *J. Cell. Mol. Med.* **23**, 5225–5234 (2019).
43. M. Onnee, P. Fanen, I. Callebaut, A. de Becdelievre, Structure-based understanding of ABCA3 variants. *Int. J. Mol. Sci.* **22**, (2021).
44. N. Cheong, M. Madesh, L. W. Gonzales, M. Zhao, K. Yu, P. L. Ballard, H. Shuman, Functional and trafficking defects in ATP binding cassette A3 mutants associated with respiratory distress syndrome. *J. Biol. Chem.* **281**, 9791–9800 (2006).
45. Y. Matsumura, N. Ban, K. Ueda, N. Inagaki, Characterization and classification of ATP-binding cassette transporter ABCA3 mutants in fatal surfactant deficiency. *J. Biol. Chem.* **281**, 34503–34514 (2006).
46. N. Weichert, E. Kaltenborn, A. Hector, M. Woischnik, A. Schams, A. Holzinger, S. Kern, M. Griese, Some ABCA3 mutations elevate ER stress and initiate apoptosis of lung epithelial cells. *Respir. Res.* **12**, 4 (2011).
47. M. Bækvad-Hansen, B. G. Nordestgaard, M. Dahl, Heterozygosity for E292V in ABCA3, lung function and COPD in 64,000 individuals. *Respir. Res.* **13**, 67 (2012).
48. Y. Matsumura, N. Ban, N. Inagaki, Aberrant catalytic cycle and impaired lipid transport into intracellular vesicles in ABCA3 mutants associated with nonfatal pediatric interstitial lung disease. *Am. J. Physiol. Lung Cell. Mol. Physiol.* **295**, L698–L707 (2008).
49. U. Schindlbeck, T. Wittmann, S. Höppner, S. Kinting, G. Liebisch, J. Hegermann, M. Griese, ABCA3 missense mutations causing surfactant dysfunction disorders have distinct cellular phenotypes. *Hum. Mutat.* **39**, 841–850 (2018).
50. N. Sever, G. Milicic, N. O. Bodnar, X. Wu, T. A. Rapoport, Mechanism of lamellar body formation by lung surfactant protein B. *Mol. Cell* **81**, 49–66.e8 (2021).
51. K. P. Locher, Mechanistic diversity in ATP-binding cassette (ABC) transporters. *Nat. Struct. Mol. Biol.* **23**, 487–493 (2016).
52. J. P. Andersen, A. L. Vestergaard, S. A. Mikkelsen, L. S. Mogensen, M. Chalat, R. S. Molday, P4-ATPases as phospholipid flippases-structure, function, and enigmas. *Front. Physiol.* **7**, 275 (2016).
53. J. D. Brunner, N. K. Lim, S. Schenck, A. Duerst, R. Dutzler, X-ray structure of a calcium-activated TMEM16 lipid scramblase. *Nature* **516**, 207–212 (2014).
54. B. F. Scharschmidt, E. B. Keeffe, N. M. Blankenship, R. K. Ockner, Validation of a recording spectrophotometric method for measurement of membrane-associated Mg- and NaK-ATPase activity. *J. Lab. Clin. Med.* **93**, 790–799 (1979).
55. D. N. Mastronarde, Automated electron microscope tomography using robust prediction of specimen movements. *J. Struct. Biol.* **152**, 36–51 (2005).
56. S. Q. Zheng, E. Palovcak, J. P. Armache, K. A. Verba, Y. Cheng, D. A. Agard, MotionCor2: Anisotropic correction of beam-induced motion for improved cryo-electron microscopy. *Nat. Methods* **14**, 331–332 (2017).
57. T. Grant, N. Grigorieff, Measuring the optimal exposure for single particle cryo-EM using a 2.6 Å reconstruction of rotavirus VP6. *eLife* **4**, e06980 (2015).
58. K. Zhang, Gctf: Real-time CTF determination and correction. *J. Struct. Biol.* **193**, 1–12 (2016).
59. J. Zivanov, T. Nakane, B. O. Forsberg, D. Kimanius, W. J. H. Hagen, E. Lindahl, S. H. W. Scheres, New tools for automated high-resolution cryo-EM structure determination in RELION-3. *eLife* **7**, e42166 (2018).
60. P. B. Rosenthal, R. Henderson, Optimal determination of particle orientation, absolute hand, and contrast loss in single-particle electron cryomicroscopy. *J. Mol. Biol.* **333**, 721–745 (2003).
61. S. X. Chen, G. M. Mullan, A. R. Faruqi, G. N. Murshudov, J. M. Short, S. H. W. Scheres, R. Henderson, High-resolution noise substitution to measure overfitting and validate resolution in 3D structure determination by single particle electron cryomicroscopy. *Ultramicroscopy* **135**, 24–35 (2013).
62. E. F. Pettersen, T. D. Goddard, C. C. Huang, G. S. Couch, D. M. Greenblatt, E. C. Meng, T. E. Ferrin, UCSF Chimera—A visualization system for exploratory research and analysis. *J. Comput. Chem.* **25**, 1605–1612 (2004).
63. P. Emsley, B. Lohkamp, W. G. Scott, K. Cowtan, Features and development of Coot. *Acta Crystallogr. D Biol. Crystallogr.* **66**, 486–501 (2010).
64. P. D. Adams, P. V. Afonine, G. Bunkóczi, V. B. Chen, I. W. Davis, N. Echols, J. J. Headd, L. W. Hung, G. J. Kapral, R. W. Grosse-Kunstleve, A. J. McCoy, N. W. Moriarty, R. Oeffner, R. J. Read, D. C. Richardson, J. S. Richardson, T. C. Terwilliger, P. H. Zwart, PHENIX: A comprehensive Python-based system for macromolecular structure solution. *Acta Crystallogr. D* **66**, 213–221 (2010).
65. C. J. Williams, J. J. Headd, N. W. Moriarty, M. G. Prisant, L. L. Videau, L. N. Deis, V. Verma, D. A. Keedy, B. J. Hintze, V. B. Chen, S. Jain, S. M. Lewis, W. B. Arendall III, J. Snoeyink, P. D. Adams, S. C. Lovell, J. S. Richardson, D. C. Richardson, MolProbity: More and better reference data for improved all-atom structure validation. *Protein Sci.* **27**, 293–315 (2018).

Acknowledgments: We thank the Cryo-EM Facility of Southern University of Science and Technology (SUSTech) for providing the facility support. The MS data were obtained using the equipment maintained by SUSTech Core Research Facilities. **Funding:** This work was supported by the National Natural Science Foundation of China (92057101 and 32122043 to X.G.), the Natural Science Foundation of Guangdong Province of China for Distinguished Young Scientists (2019B151502047 to X.G.), and the Shenzhen Science and Technology Innovation Program (RCYX20200714114522081 to X.G.). **Author contributions:** X.G. conceived and supervised the project. X.G., T.X., Z.Z., and J.Y. designed the experiments. T.X., Z.Z., J.Y., and Q.F. performed the experiments. All authors contributed to data analysis. T.X. contributed to manuscript preparation. X.G. wrote the manuscript. **Competing interests:** The authors declare that they have no competing interests. **Data and materials availability:** The EM density maps generated in this study have been deposited in the EMDB under accession codes EMD-32233 (nucleotide-free ABCA3 in GDN), EMD-32235 (nucleotide-free ABCA3 in LMNG/CHS), and EMD-32234 (ATP-bound ABCA3). The atomic coordinates have been deposited in the PDB under the accession codes 7W01 (nucleotide-free ABCA3 in GDN) and 7W02 (ATP-bound ABCA3). All data needed to evaluate the conclusions in the paper are present in the paper and/or the Supplementary Materials.

Submitted 22 November 2021
Accepted 18 February 2022
Published 8 April 2022
10.1126/sciadv.abn3727